

UC Berkeley

UC Berkeley Previously Published Works

Title

Excitation-wavelength-dependent small polaron trapping of photoexcited carriers in α -Fe₂O₃.

Permalink

<https://escholarship.org/uc/item/41q5c8xs>

Journal

Nature materials, 16(8)

ISSN

1476-1122

Authors

Carneiro, Lucas M
Cushing, Scott K
Liu, Chong
et al.

Publication Date

2017-08-01

DOI

10.1038/nmat4936

Peer reviewed

Excitation-wavelength-dependent small polaron trapping of photoexcited carriers in α -Fe₂O₃

Lucas M. Carneiro^{1,2†}, Scott K. Cushing^{1,2†}, Chong Liu^{1‡}, Yude Su¹, Peidong Yang^{1,3,4,5}, A. Paul Alivisatos^{1,3,4,5} and Stephen R. Leone^{1,2,6★}

Small polaron formation is known to limit ground-state mobilities in metal oxide photocatalysts. However, the role of small polaron formation in the photoexcited state and how this affects the photoconversion efficiency has yet to be determined. Here, transient femtosecond extreme-ultraviolet measurements suggest that small polaron localization is responsible for the ultrafast trapping of photoexcited carriers in haematite (α -Fe₂O₃). Small polaron formation is evidenced by a sub-100 fs splitting of the Fe 3p core orbitals in the Fe M_{2,3} edge. The small polaron formation kinetics reproduces the triple-exponential relaxation frequently attributed to trap states. However, the measured spectral signature resembles only the spectral predictions of a small polaron and not the pre-edge features expected for mid-gap trap states. The small polaron formation probability, hopping radius and lifetime varies with excitation wavelength, decreasing with increasing energy in the t_{2g} conduction band. The excitation-wavelength-dependent localization of carriers by small polaron formation is potentially a limiting factor in haematite's photoconversion efficiency.

Metal oxide semiconductors are promising materials for use in solar water splitting and artificial photosynthesis. In particular, haematite (α -Fe₂O₃) is an Earth-abundant semiconductor that has a visible-light bandgap in the optimal 2 eV range and is photostable, making it an ideal candidate^{1–3}. However, the lifetime of photoexcited carriers in haematite is picoseconds, not the milliseconds needed to drive water oxidation^{4–10}. Short carrier recombination lifetimes in haematite are usually assigned to surface and mid-gap trap states^{4–10}. Doping, nanostructuring, surface modifications and co-catalysts have been used to alleviate the mobility, lifetime and kinetics issues^{1–3,11–17}. However, even when trap states have been passivated, haematite's overpotential and poor fill factor issues are not fully overcome^{11,12}. Even the best performing haematite electrodes are still at-one third of their potential efficiency¹⁸.

This discrepancy in performance has recently been attributed to haematite's small polaron-limited, minority carrier conduction^{6,19,20}. When an excess charge is added to an Fe centre, the electron–optical phonon interaction causes the lattice to expand, self-trapping the carrier^{19,21}. For transport to occur, phonon motion must bring two Fe centres in proximity, giving the charge carrier a finite probability to hop between atoms. Similar to a mid-gap or surface trap state, the small polaron acts to localize the carrier to a specific site until sufficient thermal energy is present for conduction^{22–25}. Given that polaron formation is accelerated at defect sites, small polaron formation also acts to trap mobile carriers at recombination centres²¹.

While it is known that injecting a photoexcited electron from a dye to haematite creates a small polaron²⁵, it is unknown whether photoexcitation of haematite itself leads to small polaron localization. Small polaron formation should be particularly

relevant for the photoexcited state in haematite because the dominant optical transition shifts electron density from the O to Fe centre²⁶. This shift of charge density may accelerate localization of the electrons into a small polaron, decreasing mobility compared with a free carrier state and limiting photoconversion yields. While ground-state polaron transport is accepted for most metal oxide semiconductors²⁷, the role of small polarons in the photoexcited state remains unidentified.

In this paper, transient extreme-ultraviolet (XUV) spectroscopy is used to investigate small polaron localization of photoexcited carriers in haematite. Spectroscopic signatures characteristic of electron localization by small polarons are measured within 100 fs following photoexcitation. The small polaron state is found to form directly following the first optical-phonon scattering events and polaron formation continues for ~ 2 –3 ps. The small polaron formation rate versus excitation energy is found to be fastest at a visible-light excitation of 2.5 eV, but the small polaron formation probability decreases with increasing energy within the t_{2g} conduction band. The observed spectral splitting of the Fe 3p core level after photoexcitation suggests that trapping and localization of minority carriers on ultrashort timescales can be attributed to small polaron formation and not occupation of mid-gap or surface states. Further, these trends suggest that the wavelength-dependent photoconversion efficiency does not follow the increase in visible-light absorption in the t_{2g} conduction band^{1–3,14–18} because small polaron formation alters the photoexcited electron mobilities to a different extent depending on excitation energy.

Thin haematite films were prepared following ref. 26. The XUV transient absorption at the Fe M_{2,3} edge before excitation, immediately after excitation, and after polaron formation are shown in Fig. 1. The XUV absorption corresponds to the transitions

¹Department of Chemistry, University of California, Berkeley, California 94720, USA. ²Chemical Sciences Division, Lawrence Berkeley National Laboratory, Berkeley, California 94720, USA. ³Department of Materials Science and Engineering, University of California, Berkeley, California 94720, USA. ⁴Material Sciences Division, Lawrence Berkeley National Laboratory, Berkeley, California 94720, USA. ⁵Kavli Energy NanoScience Institute, Berkeley, California 94720, USA. ⁶Department of Physics, University of California, Berkeley, California 94720, USA. [†]These authors contributed equally to this work.

[‡]Present address: Department of Chemistry and Chemical Biology, Harvard University, Cambridge, Massachusetts 02138, USA. ★e-mail: srl@berkeley.edu

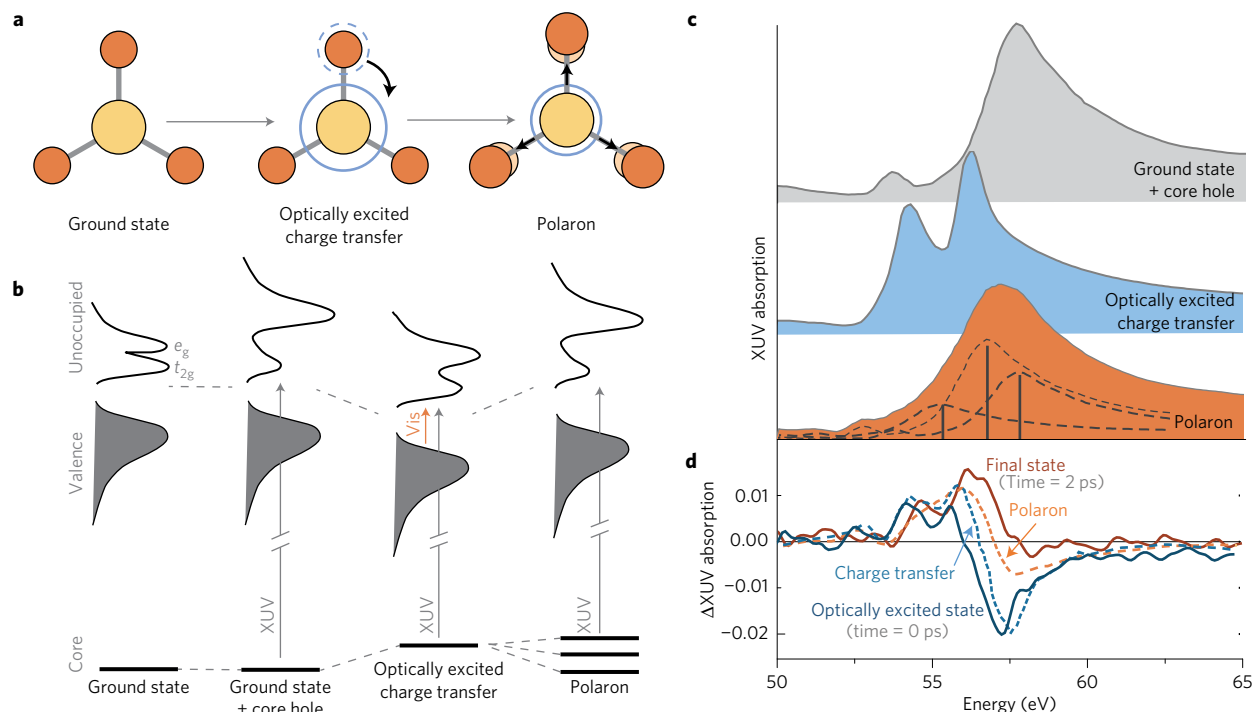


Figure 1 | Change in core level transitions with photoexcitation. a, Initial excitation of Fe₂O₃ leads to a charge-transfer transition from oxygen (dark orange) to iron (light orange). The initial excited carriers undergo optical-phonon scattering, during which the charge can be trapped in a small polaron, expanding the lattice. **b**, The XUV transition reflects the core-hole-modified unoccupied density of states (second panel) instead of the ground state (first panel). The optical charge-transfer transition changes the electronic symmetry and occupation of the Fe atom, changing the multiplet splitting measured in the XUV transition. The polaron locally changes the lattice symmetry, breaking the degeneracy of the 3p core level, and replicating the ground-state plus core-hole XUV transition to result in an overall broadened and redshifted absorption. **c**, The XUV absorption spectra of the polaron formation process. The top panel is experimental data; the bottom two panels are simulations. The multiplet splitting caused by the core hole is visible in the experimental ground-state plus core-hole absorption (first panel). The decrease in multiplet splitting after optical excitation is predicted following ref. 26 (second panel). The small polaron spectrum is predicted by splitting the experimentally measured ground state plus core hole following ref. 30 (third panel). The three contributions to the overall absorption in the polaron case are shown as dashed lines. **d**, The differential absorption predicted (dashed lines) from the difference in the spectrum of c is compared to the time = 0 ps and time = 2 ps differential absorption measurements following a 480 nm excitation pulse (solid lines).

between the Fe 3p core level and the unoccupied Fe 3d density of states as modified by the Fe 3p core hole, shown schematically in the second panel of Fig. 1b. The core-hole potential makes the XUV absorption a poor representation for the conduction band energy structure of the first panel in Fig. 1b. In particular, for the localized Fe 3d orbitals, the XUV absorbance reflects the multiplet splitting between the 3p⁶3d⁵ ground state and the 3p⁵3d⁶ XUV excited state, combined with the spin-orbit coupling of the core level, and all broadened by the core-hole lifetime²⁸.

Excitation of haematite with visible light leads to a charge-transfer transition from majority O 2p hybridized orbitals to majority Fe 3d hybridized orbitals (Fig. 1a, represented by the dashed and solid blue circles)²⁶. The shift of electron density from the O to Fe atom hybridizes the oxygen ligand's and metal centre's energy levels, with the resultant energy relaxation decreasing with increasing separation between ligand and metal energy levels²⁸. Thus, when the charge-transfer hybridized state interacts with the core hole in an XUV transition, the separation between multiplet peaks in the XUV structure is decreased compared with the ground state plus core-hole absorption (shown schematically in the second to third panel of Fig. 1b).

The change in XUV multiplet splitting with optical excitation is experimentally demonstrated by the differential absorption measured immediately following above-bandgap excitation with 480 nm light (time = 0 ps, Fig. 1d). The optical charge-transfer hybridized state appears in the differential absorption as a double-peaked, positive increase in absorption between 53 and 56 eV and

a decrease in absorption between 56 and 60 eV (ref. 26). These features correspond to the difference in multiplet peak splitting between the ground and charge-transfer hybridized state, which can be seen in Fig. 1c by comparing the experimental core-hole-modified ground-state XUV absorption to that predicted for the excited state using a charge-transfer multiplet calculation²⁹. The charge-transfer state differential absorption in Fig. 1d is calculated as the difference between the charge-transfer multiplet calculation and the ground-state absorption (see Supplementary Information for additional details regarding the charge-transfer multiplet calculation).

Small polaron formation should have two distinct effects on the photoexcited XUV spectrum³⁰. First, the small polaron creates an anisotropic expansion in the lattice as the excess charge self-traps, breaking the degeneracy of the Fe 3p levels and splitting their energies by several electronvolts (final panel of Fig. 1b). This can also be thought of as resulting from the larger radius of the Fe²⁺ to Fe³⁺ ion. Second, the small polaron-induced localization of electron density on the Fe atom decreases the charge-transfer hybridization compared with the initial optically excited state, represented by the blue circles in Fig. 1a. The small polaron therefore has a conduction band density of states that more closely resembles the ground-state Fe³⁺ atom before optical excitation than after³⁰. That is, the small polaron state resembles the Fe³⁺ state, just with new XUV transitions from the degeneracy-split core levels, leading to a spectrum that appears broadened and redshifted compared with the ground-state plus core-hole absorption (bottom panel of Fig. 1c). The small polaron's XUV spectrum can therefore be predicted by

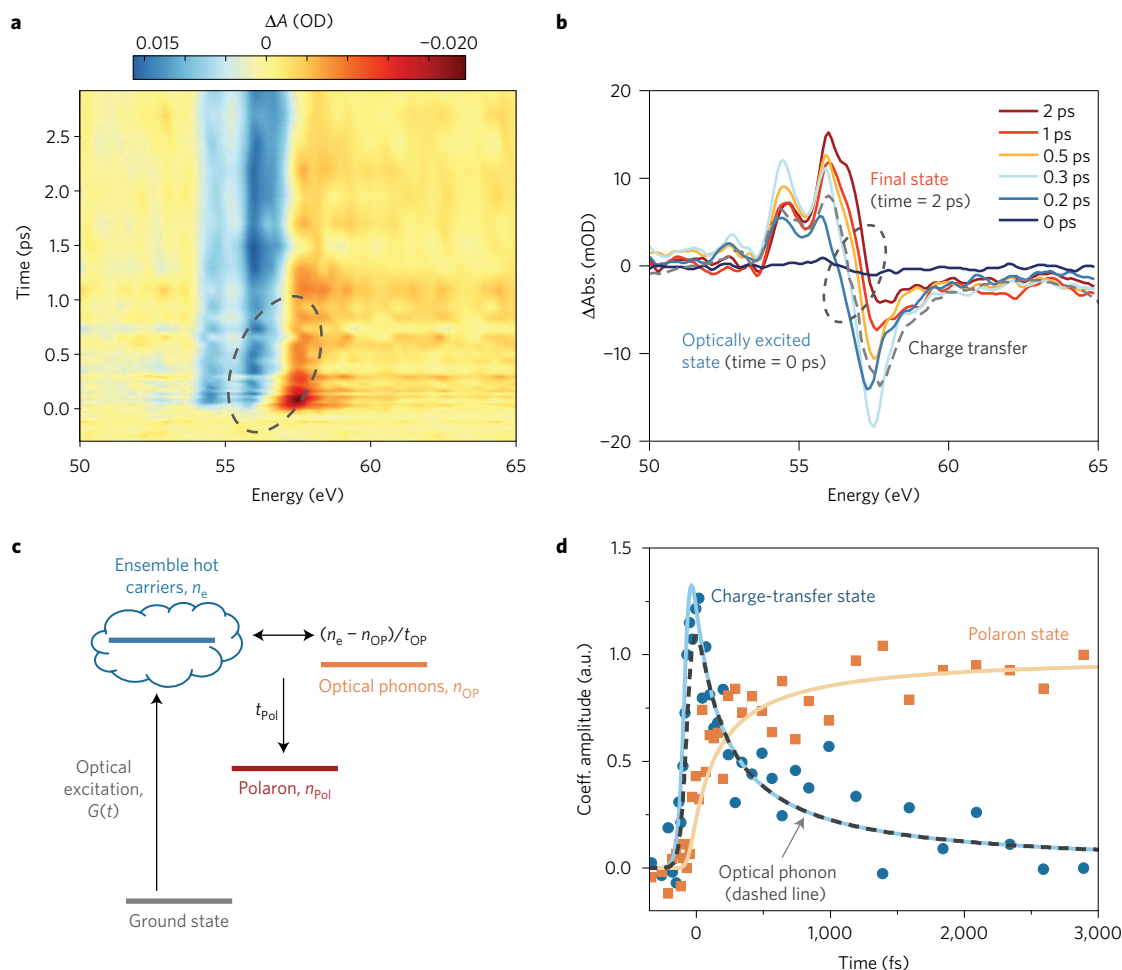


Figure 2 | Transient absorption after 480 nm excitation in Fe_2O_3 . **a**, Following excitation, the differential absorption reveals regions of increased and decreased absorption around 55 and 56 eV. The energy of the zero crossing between the areas of increased (blue) and decreased (red) absorption shifts on a 500 fs timescale and is circled for clarity. **b**, Lineouts from the full differential absorption in the experimental data, averaged over the surrounding 6 time points on a logarithmic scale to isolate the key time periods during relaxation. The shift of the zero crossing around 56–58 eV is circled and the calculated charge-transfer state is shown as a grey dashed line for reference. **c**, The rate equation model used to predict the polaron formation kinetics. Following excitation, the optically excited electrons in the charge-transfer state thermalize by scattering off of and exciting optical phonons. The optical phonon and electron can then combine to create a polaron. **d**, The experimental time = 0 ps and time = 2 ps slices are used to extract the amplitude of the charge-transfer and small polaron state using a multivariate regression of the experimental data. These amplitudes are fitted with a rate equation model for small polaron formation (solid lines). The effective phonon population that results from the rate equation model fit is shown for comparison as a dashed grey line. The phonon population is not directly measured in the experiment, so here it is scaled the same as the electron population, which would represent one electron scattering to create one phonon, which then combine to create one polaron.

convolving the ground-state plus core-hole XUV absorption with a threefold energy splitting of the $3p$ core level of 0 eV, 1 eV and 2.5 eV, using the values predicted for Fe^{3+} in FePO_4 in ref. 30.

The differential absorption at 2 ps after optical excitation is compared to the differential absorption predicted for the small polaron in Fig. 1d, confirming the presence of small polaron formation in haematite. The polaron state differential absorption in Fig. 1d is calculated as the difference between the polaron state and the ground-state absorption (see Supplementary Information for additional details regarding the polaron calculation). In both the experimental and predicted spectrum, the initial increase in absorption between 53 and 56 eV is blueshifted and the decrease in absorption at 56–60 eV is reduced, leading to a blueshift of the zero crossing between the two features. This can be visualized by comparing the predicted polaron XUV spectrum to the ground and charge-transfer hybridized XUV absorption in Fig. 1c. The blueshift of the zero crossing provides a convenient reference to monitor the small polaron formation dynamics and is circled for clarity in the full 0–3 ps experimental differential absorption in Fig. 2a and

lineouts in Fig. 2b. The lineouts in Fig. 2b are averaged over the six nearest time points on a logarithmic scale. The localization of the excited charge density is further confirmed in Supplementary Fig. 1 where the differential absorption predicted from a splitting of the $3p$ core levels in the ground state, reflecting localized electrons, is compared with that of the charge-transfer hybridized state, reflecting the photoexcited electron and hole. Carrier-induced³¹, optical phonon^{32–34} or acoustic phonon³⁵ renormalizations cannot account for the measured spectral evolution because the expected energy shifts are only on the order of ~ 100 meV compared with the several electronvolts expected for a small polaron³⁰. Neither can trap-state effects, which would lead to an additional bleach or absorption at the pre-edge of the Fe $3p$ core level around 53 eV (ref. 36), account for this. A visualization of these alternative explanations is provided in Supplementary Fig. 2 for comparison with the measured differential absorption.

The small polaron formation kinetics (Fig. 2c) can be further examined by using a multivariate regression to decompose the experimental differential absorption into the charge-transfer

hybridized and polaron states (Fig. 2d). The initial charge-transfer hybridized state is taken as the time = 0 ps differential absorption, while the final polaron state is taken as the time = 2 ps differential. The amplitude versus time from the multivariate regression is shown in Fig. 2d as circles and squares for the charge-transfer hybridized and polaron state, respectively. The charge-transfer hybridized state's amplitude rises within the 50 fs pulse width, and then decays into the small polaron state amplitude within several hundred femtoseconds. The transfer of amplitude from the hybridized state to the small polaron state stops within ~2–3 ps, indicating that small polaron formation has ceased. The residuals from the multivariate regression are reflective of the 5 mOD noise background of the experiment.

Since the small polaron formation kinetics reflect localization of the photoexcited electrons, a two-temperature rate equation model³⁷ can be adapted to simultaneously describe the hot electron–phonon equilibration while also allowing a bimolecular recombination between the hot electrons and phonons to create a small polaron (Fig. 2c). For a complete discussion of the rate equation model, the reader is referred to the Supplementary Information and Supplementary Fig. 3. In brief, the rate equation model has two rate constants that must be fitted to the experimental data for electron–phonon scattering and small polaron formation (Fig. 2c). Additionally, two amplitude coefficients must be fitted to the data to relate the change in the average population of electrons and small polarons to the amplitude in the measured transient XUV spectrum. An average population is used since the relationship between the temperature of the electrons, phonons and polarons and the resulting XUV spectral amplitudes is unknown. Using an average population ignores the momentum- and energy-specific occupation of the density of states, as well as the dependence of the electron–phonon scattering rate on energy and momentum. This approximation is justified since the transient XUV traces represent the average change in population across all occupied energy and momentum states, so fitting the kinetics gives an equally averaged electron–phonon scattering rate or polaron formation rate.

A fit to the experimental data using the rate equation model is shown as the solid lines in Fig. 2d. The fit gives an electron–phonon scattering rate of 20–30 ps^{−1} (30–60 fs) and an initial small polaron bimolecular formation rate of 11 ± 0.5 ps^{−1} (90 ± 5 fs), similar to previous reports for polaron formation^{22–24}. The competition between electron–phonon scattering to create phonons, then subsequent removal of electrons and phonons in the generation of polarons, leads to the fast rise in small polaron population followed by a slowing down of polaron formation at ~3 ps in Fig. 2d. The large uncertainty of the electron–phonon scattering rate originates in the 50 fs excitation pulse width, which represents the instrument response time and is accounted for in the fit. The extracted electron–phonon scattering rate of 20–30 ps^{−1} (30–60 fs) is consistent with inter- and intra-valley scattering in polar semiconductors where longitudinal optical phonons dominate^{38–40}, as well as with haematite's highest energy optical-phonon frequency (659 cm^{−1}; refs 41,42).

The kinetics of Fig. 2d suggests that, after excitation, the optically excited electrons in the charge-transfer hybridized state quickly scatter off of optical phonons. This optical-phonon population then begins creating small polarons on a 100 fs timescale by combining with the excited electrons. As the electron and phonon populations are consumed, the small polaron formation slows down, with the majority of electrons and optical phonons combined within ~2–3 ps following optical excitation. Although the phonon population is not directly measured, for visualization it is shown as a dashed line in Fig. 2d using the same fit amplitude as the electron population. To determine the impact of multi-phonon effects arising from excess carrier energy, the procedure of Fig. 2 was repeated for four pump wavelengths covering the visible-light absorption of

haematite (Fig. 3). The full transients, lineouts and multivariate regression-based fits are shown in Supplementary Figs 4–6.

The small polaron formation and decay process is shown schematically in Fig. 3a. The fitted small polaron formation rate versus excitation wavelength is shown in Fig. 3b and found to be fastest at 2.5 eV photoexcitation energy. The excitation wavelength dependence of the small polaron formation rate reflects the energy necessary to localize the conduction band electron and is expected to go as^{22,43,44}

$$k_{\text{st}} = Ae^{-(\Delta\varepsilon + E_{\text{rel}})^2/4E_{\text{rel}}k_{\text{B}}T} \quad (1)$$

where the prefactor *A* is related to the coupling between the mobile and localized states, $\Delta\varepsilon$ is the exothermicity of excited carriers ($E_{\text{pump}} - E_{\text{g}}$), E_{rel} is the relaxation energy associated with carrier self-trapping by polaron formation, and $k_{\text{B}}T$ is the thermal energy. Equation (1) reflects the predictions from Marcus theory, namely, if the excited carrier has too little or too much excess energy, the formation rate will increase²². Fitting equation (1) to the formation rate within the lower $t_{2\text{g}}$ conduction band⁷ gives a small polaron localization energy of -0.4 ± 0.05 eV, close to a previously measured energy of -0.3 eV (ref. 45). An elevated temperature of 600 K, roughly double the <350 K reached by optical excitation, is required to fit the data. The elevated temperature arises because equation (1) is classically derived for molecular systems and does not properly account for the optical-phonon modes in the solid²². If the formation energy is fitted considering the narrow $t_{2\text{g}}$ and e_{g} conduction bands as one band, outside the validity of equation (1), the localization energy fit is doubled to -0.6 ± 0.05 eV and the temperature fit more than quadrupled from the expected temperature to 1,600 K.

The small polaron formation probability is shown in Fig. 3c, and represented schematically in Fig. 3a in its relation to the formation rate. The polaron formation probability is calculated as the ratio between the amplitude fit coefficients, which relate the population predicted by the rate equation model to the measured transient XUV amplitudes. As the excitation energy is decreased, the amplitude fit coefficients are adjusted to reflect the number of polarons produced from the initial population of electrons. Given that the same number of electrons are excited for each pump wavelength, it would be expected that an increase in polaron formation rate would translate to either an increase in the number of polarons or no change if the electron population is rate limiting. Figure 3c demonstrates that neither case is true, as can also be seen by comparing the amplitudes of the time = 0 ps and time = 2 ps states in the kinetics of Supplementary Fig. 6, at which time the polaron formation has reached a steady state (Supplementary Figs 7 and 8). Instead, the polaron formation probability decreases with increasing energy above the $t_{2\text{g}}$ band edge, increasing again at the e_{g} band edge. This trend reflects the increasing number of optical phonons created per excited electron with excess energy above the relevant conduction band edge. This suggests that when there are more hot optical phonons present, it becomes more likely that the phonon population will re-excite or interfere with polaron formation, decreasing the formation probability. Figure 3c therefore reflects the multi-phonon effects not included in the rate equation model and suggests that faster polaron formation rates (Fig. 3b) do not necessarily lead to larger final polaron state amplitudes (Fig. 3c).

The decays of the differential absorption on a 300 ps timescale further suggest the impact of the non-thermal phonon bath. For 560 nm excitation, the differential absorption signal disappears within the noise level of the experiment by 300 ps. For 520 nm, 480 nm and 400 nm excitation, the polaron signal still exists at 300 ps (Supplementary Fig. 7), although largely reduced in amplitude, indicating decay of the polaron state. The polaron state absorption represents the excited carrier–polaron pair. The measured decay and disappearance of the polaron state, and the

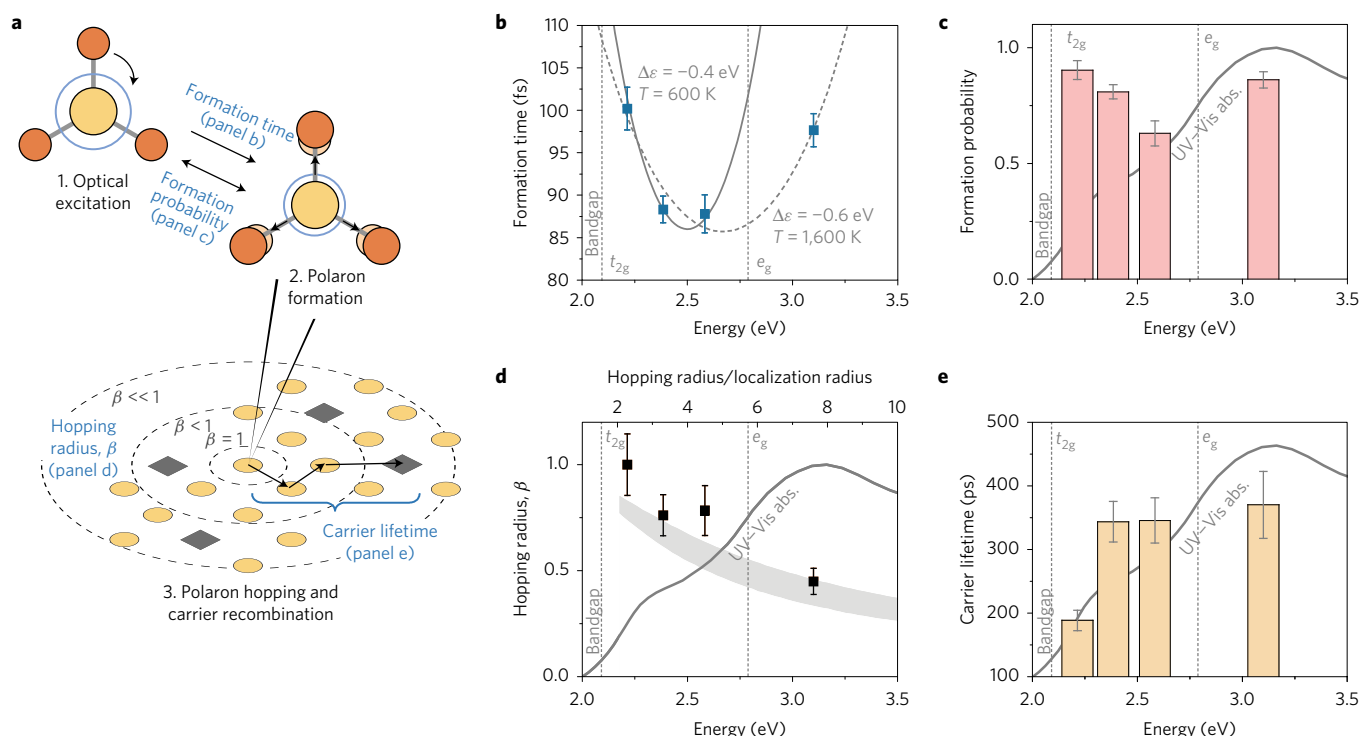


Figure 3 | Energy dependence of polaron formation and decay. **a–e**, Schematic explanation of the small polaron formation and decay (**a**), including representations of the formation time (**b**), the excitation and de-excitation process that determines the formation probability (**c**), and the hopping and recombination process (**d**) that determines the measured excited-state lifetime (**e**). **b**, The small polaron formation rate is plotted versus pump photon energy. The parabolas represent the small polaron formation energy ($\Delta\epsilon$) and effective lattice temperature within the conduction bands of α -Fe₂O₃. Fits that consider the narrow t_{2g} and e_g conduction bands as separate (solid line) and consolidated (dashed line) are shown. **c**, The relative polaron formation probability versus excitation wavelength from the rate equation model. Parts **b** and **c** reveal that at the band edge of α -Fe₂O₃ the majority of excited carriers are localized as small polarons. As the excess energy of excited carriers increases, the hot optical-phonon population increases, decreasing the effects of small polaron localization. **d**, The best-fit exponential stretching parameter versus excitation wavelength, related to the hopping radius as outlined in ref. 46. The grey area and top axis are a qualitative comparison to the predicted dependence of β on the ratio of hopping radius to localization radius from ref. 46. The grey area and top axis are a guide to the eye and are not quantitative. **e**, The best-fit lifetime from the stretched exponential model versus excitation wavelength. Parts **d** and **e** reveal that as the excitation energy is increased, the larger phonon bath promotes more hopping, resulting in a longer excited-state lifetime. In each panel the error bars represent the standard error of the best-fit parameter. The positions of the conduction band edges and the ultraviolet-visible absorption are shown for reference in **c–e**.

absence of any new spectral features such as a trap-state or charge-transfer state absorption, confirms that the excited carriers are recombining while self-trapped in the polaron.

The measured long-timescale dynamics are best-fitted using the stretched exponential theory for polaron hopping between trap states^{46,47},

$$n(t) = \exp\left(-\left(\frac{t}{\tau}\right)^\beta\right) \quad (2)$$

where t is the time, τ is the decay constant and β is the stretching parameter. The stretched exponential fit is shown in Supplementary Fig. 8 and the best-fit parameters are tabulated in Supplementary Table 1. The decay dynamics are fitted starting at the 2–3 ps timescale during which polaron formation reaches a steady state. In polaron-hopping-based decay, the stretching factor β corresponds to the possible hopping radius relative to the localization radius of the polaron (shown schematically in Fig. 3a). The stretching factor β in the exponential represents the sum over all possible hopping paths to a terminal defect site^{46,47}. When β is one, the stretched exponential reduces to an exponential decay and the excited carrier decays almost on-site with a defect-state-determined lifetime of τ . As β becomes smaller than one, more hopping paths are sampled before recombination, and the excited-state population lives longer as compared with the single-site case. In other words, the farther the

excited carrier can hop before recombination, the more the decay dynamics change from a single exponential.

In agreement with polaron-hopping theory, as excitation energy is increased in the measured data, increasing the non-thermal phonon bath, the best-fit parameter β decreases (Fig. 3d), representing increased hopping (Fig. 3a). In Fig. 3d, the grey shaded area and top axis represent qualitatively how β changes with the ratio of the hopping radius to the localization radius (adapted from ref. 46). The grey area and top axis are shown only as a trend line and are not a quantitative comparison. For 560 nm excitation, β is best-fitted to one, conveying a fast recombination with little hopping. For 400 nm excitation, the best fit of β decreases to ~ 0.4 , indicating an increased hopping radius before recombination. In agreement with the increased hopping radius, the best-fit lifetime in the stretched exponential also increases with increasing excitation energy (Fig. 3e). Figure 3d,e suggests that as the excitation energy is increased, more excess energy goes to the lattice, allowing hopping at a frequency faster than the recombination time of the occupied site. This leads to an increase of the excited-state lifetime with increasing excitation energy.

The wavelength dependence of small polaron formation across haematite's visible-light absorption, and thus the expected impact on photoconversion efficiency, can be summarized as shown in Fig. 4. Near the haematite band edge, the majority of carriers are localized as small polarons following photoexcitation. The excited

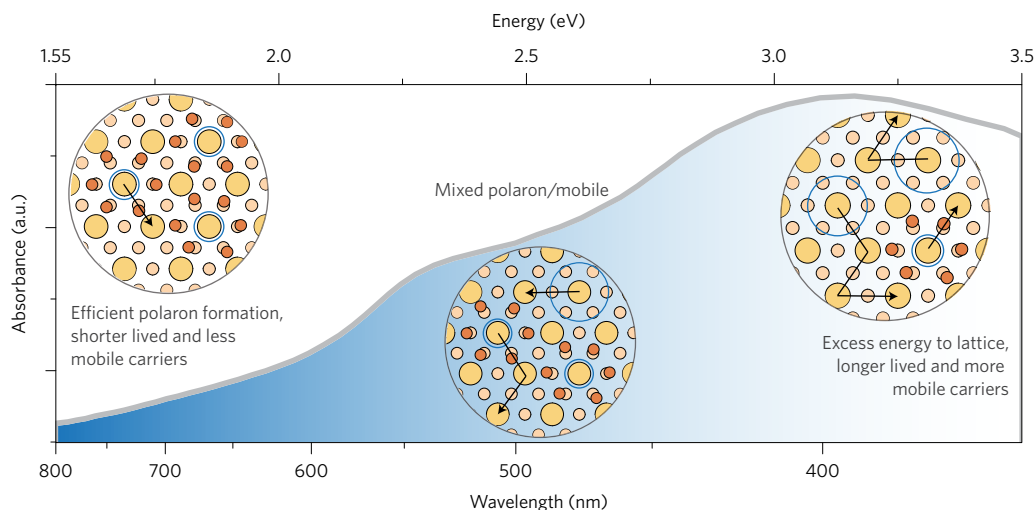


Figure 4 | Effect of polaron formation across haematite's absorption. At excitation wavelengths near the band edge, polaron formation is efficient. Excited carriers have little excess energy, so the non-thermal phonon bath is small, leading to less polaron hopping. This results in trapping of excited-state carriers, preferentially at defect sites^{21,46}, which leads to faster recombination times. As the excitation energy is increased, the excited-state polaron formation becomes less efficient, and the non-thermal phonon bath increases. This leads to an increased polaron hopping, and on average, the excited-state carriers should have a higher mobility and longer lifetime.

carriers mostly exist as polarons (Fig. 3c) and complete fewer hops before recombining (Fig. 3d). This will lead to a lower excited-state mobility and lifetime. As the excitation energy is increased, more optical phonons are created per excited carrier, and the equilibrium between mobile carriers and polarons shifts with fewer polarons being formed. As more excess energy goes to the lattice, the non-thermal phonon bath increases the hopping rate of the polaron. This leads to an increased hopping radius for the localized carrier (Fig. 3d), prolonging recombination (Fig. 3e), and increasing the average excited-state mobility. As remarked further in the discussion, these trends match the competition between recombination and charge extraction in the internal quantum efficiency for haematite⁴⁸. The internal quantum efficiency is often referred to as the absorbed photon-to-current efficiency (APCE).

The transient absorption spectra can be replicated for short timescales using only a rate equation model that incorporates bi-molecular formation of a small polaron. The transient absorption spectra can be replicated for long timescales using only a stretched exponential model that describes a random hopping terminated at a defect site. If the decay timescales are extracted at a single XUV probe energy, thus ignoring the structure of the XUV spectrum, the data can be fitted with a triple-exponential model. For example, the time constants obtained from a fit at an energy of 57.5 eV (peak of the bleach) following 480 nm excitation are 78 ± 16 fs, 1.6 ± 0.1 ps and >100 ps. These time constants reflect those reported in the visible-light transient absorption literature^{4–10}, which are commonly attributed to hot electron relaxation (~ 100 fs), followed by trapping (~ 1 ps), and finally relaxation back to the ground state (~ 100 ps). However, within the experimental noise, the measured differential XUV spectrum does not have the pre-edge increase or decrease in absorption around 53 eV that would be associated with trap or mid-gap states³⁶, nor can it be reproduced by triple-exponential recombination of the charge-transfer hybridized state alone (Supplementary Fig. 2). The polaron state is measured to persist through the decay of the differential absorption. While defect states themselves undeniably affect the photoconversion efficiency, most likely serving as the recombination sites in the random walk of the hopping polaron^{21,46}, the results here suggest that small polarons are primarily responsible for the ultrafast trapping processes and decreased mobility measured in haematite, and not the mid-gap or surface states themselves. The critical difference is that even when trap

states are passivated, small polaron localization will still exist, acting as an upper bound on the photoconversion efficiency in haematite.

The results of this paper therefore support recent suggestions^{6,19,20} that small polaron formation is what is limiting bulk transport and recombination in even the highest efficiency haematite photoelectrodes to date. If photoexcited carriers are not trapped as a small polaron, their mobility is determined by the curvature of the energy band and the resultant effective mass, just as in most semiconductors. Once localized as a small polaron, however, the effective mass greatly increases and transport occurs by thermally activated hopping, most often terminating at defect sites^{21,46}.

The limiting effect of small polarons may be further evidenced in that the photoconversion efficiency of haematite^{1–3,11,14–17} does not increase proportionately with the optical absorption near 2.1–2.5 eV (500–600 nm) in the t_{2g} conduction band, it then peaks near 2.5 to 3 eV (400–450 nm), and drops or levels off for higher excitation in the e_g band. This is best visualized by examining the APCE for haematite such as shown in ref. 48. The APCE represents the internal quantum efficiency, or the competition between charge extraction and recombination for a photoexcited carrier. For excitation wavelengths near haematite's band edge, small polaron formation is largest, and a smaller hopping radius is measured before recombination. The average carrier lifetime and mobility will therefore be smaller, decreasing the internal quantum efficiency in agreement with the APCE⁴⁸. As the excitation energy is increased, small polaron formation decreases, and the hopping and excited-state lifetime increases. The average carrier lifetimes and mobility will therefore be improved compared with band-edge excitation, increasing the internal quantum efficiency, again in agreement with the APCE⁴⁸. In other words, these results indicate that the photoconversion efficiency will deviate from the optical absorption trend at excitation wavelengths where small polaron formation is high and the small polaron's hopping rate is low.

Methods

Methods, including statements of data availability and any associated accession codes and references, are available in the [online version of this paper](#).

Received 17 January 2017; accepted 26 May 2017;
published online 10 July 2017

References

- Lin, Y., Yuan, G., Sheehan, S., Zhou, S. & Wang, D. Hematite-based solar water splitting: challenges and opportunities. *Energy Environ. Sci.* **4**, 4862–4869 (2011).
- Sivula, K., Le Formal, F. & Grätzel, M. Solar water splitting: progress using hematite (α -Fe₂O₃) photoelectrodes. *ChemSusChem* **4**, 432–449 (2011).
- Tamir, A. G., Rick, J., Dubale, A. A., Su, W. N. & Hwang, B. J. Using hematite for photoelectrochemical water splitting: a review of current progress and challenges. *Nanosci. Horiz.* **1**, 243–267 (2016).
- Cherepy, N. J., Liston, D. B., Lovejoy, J. A., Deng, H. & Zhang, J. Z. Ultrafast studies of photoexcited electron dynamics in γ - and α -Fe₂O₃ semiconductor nanoparticles. *J. Phys. Chem. B* **102**, 770–776 (1998).
- Barroso, M., Pendlebury, S. R., Cowan, A. J. & Durrant, J. R. Charge carrier trapping, recombination and transfer in hematite (α -Fe₂O₃) water splitting photoanodes. *Chem. Sci.* **4**, 2724–2734 (2013).
- Pendlebury, S. R. *et al.* Ultrafast charge carrier recombination and trapping in hematite photoanodes under applied bias. *J. Am. Chem. Soc.* **136**, 9854–9857 (2014).
- Sorenson, S., Driscoll, E., Haghighat, S. & Dawlaty, J. M. Ultrafast carrier dynamics in hematite films: the role of photoexcited electrons in the transient optical response. *J. Phys. Chem. C* **118**, 23621–23626 (2014).
- Joly, A. G. *et al.* Carrier dynamics in α -Fe₂O₃ (0001) thin films and single crystals probed by femtosecond transient absorption and reflectivity. *J. Appl. Phys.* **99**, 053521 (2006).
- Fitzmorris, B. C. *et al.* Ultrafast transient absorption studies of hematite nanoparticles: the effect of particle shape on exciton dynamics. *ChemSusChem* **6**, 1907–1914 (2013).
- Nadtochenko, V. A. *et al.* Femtosecond relaxation of photoexcited states in nanosized semiconductor particles of iron oxides. *Russ. Chem. Bull. Int. Ed.* **51**, 457–461 (2002).
- LeFormal, F. *et al.* Back electron–hole recombination in hematite photoanodes for water splitting. *J. Am. Chem. Soc.* **136**, 2564–2574 (2014).
- Braun, A. *et al.* Direct observation of two electron holes in a hematite photoanode during photoelectrochemical water splitting. *J. Phys. Chem. C* **116**, 16870–16875 (2012).
- Zandi, O. & Hamann, T. W. The potential versus current state of water splitting with hematite. *Phys. Chem. Chem. Phys.* **17**, 22485–22503 (2015).
- Gui, Q. *et al.* Enhanced photoelectrochemical water splitting performance of anodic TiO₂ nanotube arrays by surface passivation. *ACS Appl. Mater. Interfaces* **6**, 17053–17058 (2014).
- Cesar, I., Sivula, K., Kay, A., Zboril, R. & Grätzel, M. Influence of feature size, film thickness, and silicon doping on the performance of nanostructured hematite photoanodes for solar water splitting. *J. Phys. Chem. C* **113**, 772–782 (2008).
- Sivula, K. Metal oxide photoelectrodes for solar fuel production, surface traps, and catalysis. *J. Phys. Chem. Lett.* **4**, 1624–1633 (2013).
- Ling, Y. & Li, Y. Review of Sn-doped hematite nanostructures for photoelectrochemical water splitting. *Part. Part. Syst. Charact.* **31**, 1113–1121 (2014).
- Shen, S., Lindley, S. A., Chen, X. & Zhang, J. Z. Hematite heterostructures for photoelectrochemical water splitting: rational materials design and charge carrier dynamics. *Energy Environ. Sci.* **9**, 2744–2775 (2016).
- Rettie, A. J., Chemelewski, W. D., Emin, D. & Mullins, C. B. Unravelling small-polaron transport in metal oxide photoelectrodes. *J. Phys. Chem. Lett.* **7**, 471–479 (2016).
- Warren, S. C. *Photoelectrochemical Hydrogen Production* 293–316 (Springer, 2012).
- Emin, D. *Condensed Matter Physics* 16–34 (Springer, 1987).
- Ge, N. H. *et al.* Femtosecond dynamics of electron localization at interfaces. *Science* **279**, 202–205 (1998).
- Wang, T., Caraianni, C., Burg, G. W. & Chan, W. L. From two-dimensional electron gas to localized charge: dynamics of polaron formation in organic semiconductors. *Phys. Rev. B* **91**, 041201 (2015).
- Muntwiler, M. & Zhu, X. Y. Formation of two-dimensional polarons that are absent in three-dimensional crystals. *Phys. Rev. Lett.* **98**, 246801 (2007).
- Katz, J. E. *et al.* Electron small polarons and their mobility in iron (oxyhydr) oxide nanoparticles. *Science* **337**, 1200–1203 (2012).
- Vura-Weis, J. *et al.* Femtosecond M₂₃-edge spectroscopy of transition-metal oxides: photoinduced oxidation state change in α -Fe₂O₃. *J. Phys. Chem. Lett.* **4**, 3667–3671 (2013).
- Bosman, A. J. & Van Daal, H. J. Small-polaron versus band conduction in some transition-metal oxides. *Adv. Phys.* **19**, 1–117 (1970).
- De Groot, F. & Kotani, A. *Core Level Spectroscopy of Solids* 133–142 (CRC, 2008).
- Stavitski, E. & de Groot, F. M. F. The CTM4XAS program for EELS and XAS spectral shape analysis of transition metal L edges. *Micron* **41**, 687–694 (2010).
- Wang, Z. & Bevan, K. H. Exploring the impact of semicore level electronic relaxation on polaron dynamics: an adiabatic *ab initio* study of FePO₄. *Phys. Rev. B* **93**, 024303 (2016).
- Tränkle, G. *et al.* Dimensionality dependence of the band-gap renormalization in two- and three-dimensional electron–hole plasmas in GaAs. *Phys. Rev. Lett.* **58**, 419–422 (1987).
- Rethfeld, B., Sokolowski-Tinten, K., Von Der Linde, D. & Anisimov, S. I. Timescales in the response of materials to femtosecond laser excitation. *Appl. Phys. A* **79**, 767–769 (2004).
- Stampfli, P. & Bennemann, K. H. Theory for the laser-induced femtosecond phase transition of silicon and GaAs. *Appl. Phys. A* **60**, 191–196 (1995).
- Bennett, B. R., Soref, R. A. & Del Alamo, J. A. Carrier-induced change in refractive index of InP, GaAs and InGaAsP. *IEEE J. Quant. Electron.* **26**, 113–122 (1990).
- Rose-Petruck, C. *et al.* Picosecond–milliångström lattice dynamics measured by ultrafast X-ray diffraction. *Nature* **398**, 310–312 (1999).
- Santomauro, F. G. *et al.* Femtosecond X-ray absorption study of electron localization in photoexcited anatase TiO₂. *Sci. Rep.* **5**, 14834 (2015).
- Van Driel, H. M. Kinetics of high-density plasmas generated in Si by 1.06- and 0.53- μ m picosecond laser pulses. *Phys. Rev. B* **35**, 8166–8176 (1987).
- Becker, P. C. *et al.* Femtosecond intervalley scattering in GaAs. *Appl. Phys. Lett.* **53**, 2089–2090 (1988).
- Lin, W. Z., Schoenlein, R. W., Fujimoto, J. G. & Ippen, E. P. Femtosecond absorption saturation studies of hot carriers in GaAs and AlGaAs. *IEEE J. Quant. Electron.* **24**, 267–275 (1988).
- Fluegel, B. D. *et al.* Experimental and theoretical investigation of femtosecond carrier relaxation in CdSe. *Solid State Commun.* **83**, 17–19 (1992).
- Shim, S.-H. & Duffy, T. S. Raman spectroscopy of Fe₂O₃ to 62 GPa. *Am. Mineral.* **87**, 318–326 (2001).
- Jubb, A. M. & Allen, H. C. Vibrational spectroscopic characterization of hematite, maghemite, and magnetite thin films produced by vapor deposition. *ACS Appl. Mater. Interfaces* **2**, 2804–2812 (2010).
- Holstein, T. Studies of polaron motion. *Ann. Phys., NY* **8**, 325–342 (1959).
- Marcus, R. A. & Sutin, N. Electron transfers in chemistry and biology. *BBA Rev. Bioenerg.* **811**, 265–322 (1985).
- Peng, H. & Lany, S. Semiconducting transition-metal oxides based on d⁵ cations: theory for MnO and Fe₂O₃. *Phys. Rev. B* **85**, 201202 (2012).
- Sturman, B., Podivilov, E. & Gorkunov, M. Origin of stretched exponential relaxation for hopping-transport models. *Phys. Rev. Lett.* **91**, 176602 (2003).
- Merschjann, C., Imlau, M., Brüning, H., Schoke, B. & Torbrügge, S. Nonexponential relaxation dynamics of localized carrier densities in oxide crystals without structural or energetic disorder. *Phys. Rev. B* **84**, 052302 (2011).
- Lin, Y., Zhou, S., Sheehan, S. W. & Wang, D. Nanonet-based hematite heteronanostructures for efficient solar water splitting. *J. Am. Chem. Soc.* **133**, 2398–2401 (2011).

Acknowledgements

This work was supported by the US Department of Energy, Office of Science, Office of Basic Energy Sciences, Materials Sciences and Engineering Division, under Contract No. DE-AC02-05-CH11231 within the Physical Chemistry of Inorganic Nanostructures Program (KC3103). S.K.C. acknowledges support by the Department of Energy, Office of Energy Efficiency and Renewable Energy (EERE) Postdoctoral Research Award under the EERE Solar Energy Technologies Office.

Author contributions

L.M.C., S.K.C. and S.R.L. designed the study. L.M.C. and S.K.C. performed the transient XUV measurements and data analysis. S.K.C. modelled the polaron spectral signature and dynamics. C.L. and Y.S. were responsible for sample fabrication and characterization. L.M.C., S.K.C., C.L., Y.S., P.Y., A.P.A. and S.R.L. wrote and revised the manuscript.

Additional information

Supplementary information is available in the online version of the paper. Reprints and permissions information is available online at www.nature.com/reprints. Publisher's note: Springer Nature remains neutral with regard to jurisdictional claims in published maps and institutional affiliations. Correspondence and requests for materials should be addressed to S.R.L.

Competing financial interests

The authors declare no competing financial interests.

Methods

Sample fabrication. The α -Fe₂O₃ thin films were deposited onto 30 nm Si₃N₄ substrates by radiofrequency magnetron sputtering of ~ 10 nm of iron metal, and subsequent oxidation in ambient atmosphere in a tube furnace at 500 °C for 1 h, followed by natural cooling to room temperature. The resonant M_{2,3}-edge absorption of the samples has two peaks at 55 eV and 57 eV in agreement with literature values for thin-film α -Fe₂O₃. Authors of ref. 26 prepared α -Fe₂O₃ thin-film samples using the same process and confirmed the α phase composition through electron diffraction measurements from ref. 49.

Transient extreme-ultraviolet (XUV) spectroscopy. Transient XUV pulses were created using a 1 kHz Ti:sapphire chirped pulse amplifier (Spitfire Pro, Spectra Physics) generating 40 fs, 3.5 mJ pulses centred at 800 nm. The XUV spectrum is produced using high harmonic generation in a 40-cm-long semi-infinite gas cell filled with 80 torr of neon. The spot size of the focused beam is about 100 μ m, giving a peak intensity of 5.7×10^{14} W cm⁻². Twenty microjoules of 400 nm light was mixed with the 800 nm fundamental to generate both odd- and even-order harmonics. A 0.6- μ m-thick Al foil is employed to block any residual 800 nm and 400 nm light from reaching the sample. The XUV pulses were spectrally dispersed

by a variable line spacing grating onto a CCD (charge-coupled device) camera (PIXIS-400, Princeton Instruments). The spectrometer has an energy range of 38–80 eV and a spectral resolution of ~ 150 meV. An optical parametric amplifier (TOPAS-Prime, Light Conversion) was used to excite the sample. The pump beam spot size at the sample is ~ 150 μ m, and the pump power was adjusted to create a carrier density of 8×10^{19} cm⁻³ at each excitation wavelength. To avoid thermally induced damage, each 3 mm \times 3 mm sample is raster scanned by 100 μ m step sizes between each pump–probe time delay measurement. To avoid artefacts caused by scattering of residual pump beam, spectra taken with the XUV pulse arriving 500 fs before the pump pulse are subtracted from the spectra at each pump–probe time delay. Detailed descriptions of the excited state XUV predictions are available in the Supplementary Information.

Data availability. The source data necessary to support the findings of this paper are available from the corresponding author upon request.

References

49. Gialanella, S. *et al.* On the goethite to hematite phase transformation. *J. Therm. Anal. Calorim.* **102**, 867–873 (2010).